

## Micro-computed tomography image-based evaluation of 3D anisotropy degree of polymer scaffolds

Úrsula Pérez-Ramírez<sup>a</sup>, Jesús Javier López-Orive<sup>a</sup>, Estanislao Arana<sup>b</sup>, Manuel Salmerón-Sánchez<sup>c</sup> and David Moratal<sup>a\*</sup>

<sup>a</sup>Centre for Biomaterials and Tissue Engineering, Universitat Politècnica de València, Valencia, Spain; <sup>b</sup>Department of Radiology, Fundación Instituto Valenciano de Oncología, Valencia, Spain; <sup>c</sup>Division of Biomedical Engineering, School of Engineering, University of Glasgow, Glasgow, UK

(Received 7 June 2012; final version received 19 June 2013)

Anisotropy is one of the most meaningful determinants of biomechanical behaviour. This study employs micro-computed tomography ( $\mu$ CT) and image techniques for analysing the anisotropy of regenerative medicine polymer scaffolds. For this purpose, three three-dimensional anisotropy evaluation image methods were used: ellipsoid of inertia (EI), mean intercept length (MIL) and tensor scale (t-scale). These were applied to three patterns (a sphere, a cube and a right prism) and to two polymer scaffold topologies (cylindrical orthogonal pore mesh and spherical pores). For the patterns, the three methods provided good results. Regarding the scaffolds, EI mistook both topologies (0.0158,  $[-0.5683; 0.6001]$ ; mean difference and 95% confidence interval), and MIL showed no significant differences (0.3509,  $[0.0656; 0.6362]$ ). T-scale is the preferable method because it gave the best capability (0.3441,  $[0.1779; 0.5102]$ ) to differentiate both topologies. This methodology results in the development of non-destructive tools to engineer biomimetic scaffolds, incorporating anisotropy as a fundamental property to be mimicked from the original tissue and permitting its assessment by means of  $\mu$ CT image analysis.

**Keywords:** anisotropy analysis; ellipsoid of inertia; image analysis; mean intercept length; polymer scaffolds; tensor scale

### Introduction

Polymer scaffolds of different architectures are commonly synthesised to obtain effective functional biological responses in tissue engineering strategies, avoiding problems of donor site scarcity, immune rejection and pathogen transfer. Such structures are designed to behave as an extracellular matrix where cells may deposit and organise into an architecture, stimulating the formation of new tissues and defining their ultimate shape and size (Langer and Vacanti 1993; Hutmacher 2000).

Tissue engineering techniques are focused on the design of scaffolds that match biological and physiochemical properties of the tissue where they are settled. However, the control of these synthesised scaffold characteristics in the fabrication process still remains a great challenge in tissue engineering (Hollister 2005; Engelmayer et al. 2006; Treharne et al. 2011).

Several methods have been developed for the synthesis of a three-dimensional (3D) polymer scaffold with different structural properties regarding network topology, pore shape, pore size and density, aiming to achieve an optimal biological and mechanical functional response (Mikos et al. 1993; Thomson et al. 1995; Harris et al. 1998; Gao et al. 2003; Zhou et al. 2005; Giardino et al. 2006; Moroni et al. 2006; Bokhari et al. 2007; Salerno et al. 2008; Terrier et al. 2009; Subramanian et al. 2011). One important

characteristic of several tissues, e.g. bone, cartilage and muscle, is that they are geometrically anisotropic in nature, which leads to a significant dependence of their mechanical properties on the spatial direction, i.e. anisotropic mechanical properties. Moreover, external mechanical loads are spatially and temporary variable within the tissues, which makes anisotropy a fundamental property to be understood in terms of not only geometry, but also of the mechanical response of musculoskeletal tissues (Wald et al. 2007). When synthetic scaffolds are designed seeking to substitute this sort of tissues, making use of tissue engineering techniques based on biomimetic grounds, the original anisotropy has to be accounted for in the engineered system (Li et al. 2007; Garrigues et al. 2010; Bonani et al. 2011; Cai et al. 2011). However, the assessment of the 3D scaffold structural anisotropy is mostly limited to measure its reflection into some mechanical properties, by performing experiments on several synthesised systems that are destroyed after each assay, and allows one to obtain limited information on the system. Anisotropy is usually tested in a compressive device that allows us to determine the compressive modulus and the elastic collapse stress in three perpendicular directions (Mathieu et al. 2006).

In contrast, the goal in musculoskeletal tissue engineering is to mimic the geometrical and functional

\*Corresponding author. Email: [dmoratal@eln.upv.es](mailto:dmoratal@eln.upv.es)

properties of tissues to engineer structures, which, needless to say, must consider the incorporation of 3D structural anisotropy as a whole (Li et al. 2007). To do so, it is of utmost importance to develop adequate tools to quantify the geometrical anisotropy of the designed 3D structure and its relationship with the expected mechanical properties *in silico*, that is to say in a non-invasive, comparable and objective way.

Micro-computed tomography ( $\mu$ CT) scanners allow for the non-destructive, non-invasive and quantitative examination of scaffolds at a high spatial resolution (Ho and Hutmacher 2006). In addition, the recent application of advanced image processing algorithms and simulation-based computational methods, such as the finite element method to  $\mu$ CT acquisitions, permits the texture and virtual mechanical analysis of 3D scaffold architecture (Alberich-Bayarri et al. 2009).

Regarding anisotropy, several studies have been conducted. Ellipse of inertia in two dimensions (2D) and ellipsoid of inertia (EI) in its 3D version are based on physical and mechanical fundamentals. They consist of a representation related to the moment of inertia. To analyse the anisotropy of trabecular bones, Yi et al. (2007) used the fractal geometry technique. The power spectrum was employed to calculate the fractal dimensions of the trabecular bone, and a polar plot of directional fractal dimensions was defined as an ellipse of inertia. The earliest and still most widely employed method is the mean intercept length (MIL), which was introduced first in 2D (Whitehouse 1974) and was defined with respect to an orientation as the mean distance between a change from one phase to other in such an orientation (Gomberg et al. 2003; Inglis and Pietruszczak 2003). Ten years later (Harrigan and Mann 1984), the concept was extended to a 3D space. On the other hand, it initiated the notion of a local morphometric scale using a spherical model (Saha et al. 2000; Saha and Udupa 2001), but it ignored orientation and anisotropy of local structures. Later, the 2D tensor scale (t-scale) appeared (Saha 2003), providing a unified parametric representation of local structure orientation, anisotropy and thickness. Regional structure was represented by a local best-fit ellipse, and its eccentricity determined anisotropy. One year later, the t-scale was extended to 3D (Saha and Wehrli 2004a). The method has been found to be remarkably robust over a wide range of resolution regimes (Saha 2005; Wehrli 2007; Xu et al. 2009, 2011), and thus it could also be applicable to  $\mu$ CT imaging.

The three described techniques for anisotropy characterisation are developed and implemented for the present work in their 3D versions, being the main purpose of this study to present and apply a methodology for a robust anisotropy degree analysis that classifies two different structures of synthesised polymer scaffolds. Only the anisotropy index will be considered for this

classification as the directional information that could be obtained through the anisotropy tensor is not relevant for this purpose.

The results of the analysis add relevant information to the non-destructive characterisation of scaffolds in terms of fabric anisotropy and design reliability.

## Materials and methods

### *Simulated 3D patterns*

Three well-known greyscale and binary simple 3D patterns were built using MATLAB R2010a software (The Mathworks, Natick, MA, USA). They consisted of an isotropic sphere with a diameter of 30 pixels, an isotropic cube (following the Cartesian axes) of 20 pixels of side and an anisotropic prism whose ratio between axes was 1:1:2 with the largest axis measuring 20 pixels. Despite focusing on meshes and grids, solid objects without holes are simulated and analysed for verification of the developed methods as the relationship of its axes establishes their anisotropy index, and this can be easily determined theoretically.

### *Preparation of the polymer synthesised scaffolds*

#### *Constructs using a cylindrical orthogonal pore mesh*

Ethyl acrylate (Aldrich, Barcelona, Spain, 99% pure) was employed without further purification. Ethylene glycol dimethacrylate (EGDMA; 1 wt.%) and Azobisisobutyronitrile (AIBN; 0.1 wt.%) were used as a cross-linker agent and thermal initiator, respectively. The monomeric solution polymerised undergoing bulk free radical polymerisation when the temperature was raised up to 70°C for 24 h.

A detailed procedure regarding the obtaining of this pore architecture is explained elsewhere (Rodríguez Hernández et al. 2008). Briefly, a fixed number of polyamide 6.6 sheets of commercial textile fabrics (SAATI S.A., Barcelona, Spain) were useful in building well-ordered structures to serve as porogenic templates. The nominal thread diameters of the employed fabrics were 80  $\mu$ m (D80) and 150  $\mu$ m (D150).

The fabrics underwent a two-step process, which included compression and sintering of 25 stacked sheets. The immersion of the produced templates into the monomeric solution enabled the filling of the available spaces within the templates. After polymerisation, a material was formed in which the polyamide template was embedded. The polyamide 6 template was then dissolved by immersion in nitric acid (Aldrich, 60% extra pure). After the removal of the template, the resulting porous materials were rinsed in boiling ethanol so as to remove any remaining chemicals. Finally, the scaffolds were dried *in vacuo* at 70°C to a constant weight.

### Constructs with spherical pores

Caprolactone 2-(methacryloyloxy) ethyl ester (CLMA) (Aldrich) and 2-hydroxyethyl acrylate (HEA) (Sigma-Aldrich, Madrid, Spain, 96% pure) were also used without additional treatment. Benzoin (Aldrich, 98% pure) and EGDMA (Aldrich, 99% pure) were used as initiator and cross-linking agent, respectively. Acetone (Scharlau, Barcelona, Spain, 99% pure) and ethanol (Aldrich, 99.5% pure) were responsible for the solution.

A detailed procedure regarding obtaining this pore architecture is explained elsewhere (Escobar Ivirico et al. 2007). Poly(methyl methacrylate) (PMMA) microspheres of known size ( $90 \pm 10 \mu\text{m}$ , Colacryl, Durham, UK), employed as porogen, were introduced between two plates and heated at  $180^\circ\text{C}$  for half an hour to obtain the first template. In order to obtain scaffolds with controlled porosity, a series of templates with varying degrees of compression were prepared. After cooling the template to room temperature (rt.), a monomer solution (in different weight proportions of both components 100/0 [CLMA], 70/30 [CLMA70], 50/50 [CLMA50], 30/70 [CLMA30] CLMA/HEA) was introduced in the empty space between the PMMA spheres. The polymerisation was carried out up to limiting conversion under an ultraviolet radiation source at rt.. After the polymerisation took place, the PMMA matrix was removed by soxhlet extraction using acetone (Scharlau, synthesis grade). At that stage, the PMMA porogen template was completely removed. The porous sample was kept for 24 h more in a soxhlet with ethanol to extract substances of low molecular weight. Samples were dried in vacuum until constant weight (differences below 1%) before characterisation.

Figure 1(a),(b) shows a scanning electron microscopy image of the different polymer scaffolds for regenerative medicine analysed in this work, where the different topologies can be observed (cylindrical orthogonal pore mesh and interconnected spherical pores).

### $\mu\text{CT}$ acquisitions

The  $\mu\text{CT}$  images were acquired in a high resolution *in vitro* scanner Sky-Scan1072 (Bruker, Kontich, Belgium). The specimens were mounted on a rotary stage and scanned for a complete rotation of  $360^\circ$  using an X-ray tube voltage of 40 kV. The images were a series of 124–184 slices of  $1024 \times 1024$  pixels with an isotropic spatial resolution of  $7.13 \mu\text{m}$ . Six scaffold series have been employed: concretely, four constructs with a cylindrical orthogonal pore mesh (CLMA, CLMA70, CLMA50 and CLMA30) and two constructs with spherical pores (D80 and D150).

### Image processing

All image processing was carried out using MATLAB R2010a. An initial preparation of the images was required

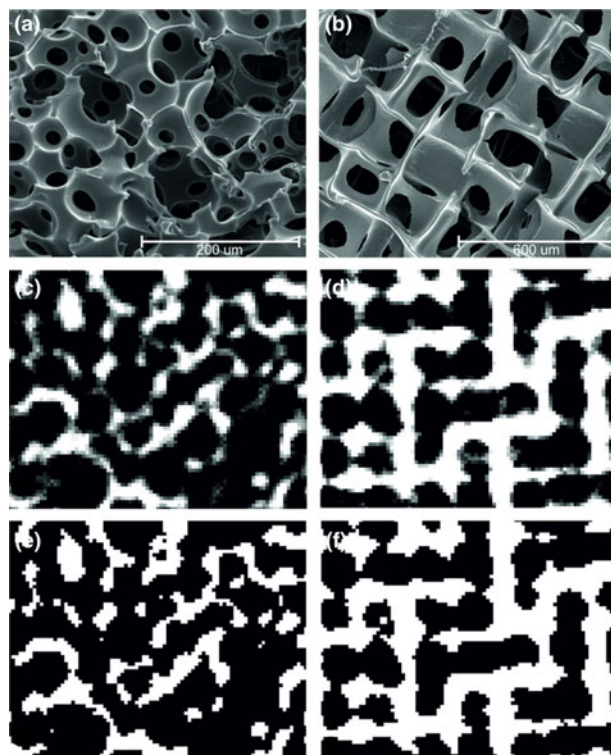


Figure 1. Different polymer scaffolds structures: (a, c and e) interconnected spherical pores (CLMAx scaffolds); (b, d and f) cylindrical orthogonal pore mesh (Dx scaffolds). (a, b) Scanning electron microscopy of the different structures. (c, d) Greyscaled scaffold  $\mu\text{CT}$  image. (e, f) Binarised image of (c) and (d), respectively, by means of Otsu's method.

before the application of the algorithms for structure analysis. The processing algorithms applied to the images are listed below and are similar to those specified in Alberich-Bayarri et al. (2009).

### Segmentation

A square region of interest (ROI) was selected in each slice by an automated algorithm to process a representative sample of the scaffold. It was of approximately  $300 \times 300$  pixels for the CLMA scaffolds and  $400 \times 400$  pixels for the spherical pore constructs. Resultant greyscale images were stored in a 3D matrix representing a 3D reconstruction of the specified volume of interest (VOI) of the scaffold. Segmented volumes were checked to exclusively contain air and structure, excluding boundary regions which could add errors to the measurements.

### Binarisation

The different greyscale  $\mu\text{CT}$  slices were binarised using the Otsu's method (Otsu 1979) as shown in Figure 1, which is a non-parametric and unsupervised method of



automatic threshold selection from a grey-level histogram. This procedure employs statistical techniques so that the intra-class variance is minimised in the whole volume maximising at the same time the inter-class variance. It is necessary to define the number of levels, in this case two, and the image is automatically divided into so many grey levels as indicated. The method was implemented in 3D and followed the expression in Equation (1):

$$t_{\text{vol}}^* = \arg \cdot \max_t \frac{\sigma_B^2}{\sigma_T^2}, \quad (1)$$

where  $\sigma_T^2$  is the total variance and  $\sigma_B^2$  is the between-class variance. The optimal binarisation threshold for the volume is  $t_{\text{vol}}^*$ . Then, the voxels were classified as belonging to structure or air depending on their intensity value. Finally, a 3D logical matrix containing the scaffold structure resulted from the application of the binarisation process.

### Anisotropy degree analysis

Three different methods were developed and implemented for the anisotropy degree characterisation of the scaffolds and the evaluation of their reproducibility and robustness. Both patterns and  $\mu$ CT scaffold images were analysed following exactly the same methodology.

### Ellipse and EI

Inertia is the resistance of a body to change its state of rest or motion. It depends solely on the mass distribution, and it is fully characterised by the tensor of inertia – whose elements are the moments of inertia with respect to the orthonormal axes of the Cartesian coordinate system – and the products of inertia. The moment of inertia along with the properties of the material determines the maximum resistance of a structural element under bending stresses. The graphical representation of the tensor of inertia is the EI (or the ellipse of inertia in 2D). The calculation of this surface is done with respect to an origin of the reference system, O, usually placed at the centre of mass, and it allows the computation for the moment of inertia relative to any axis going through O. Thus, the moment of inertia  $I_{OL}$  of the body with respect to the axis OL is calculated as  $\int p^2 dm$ , where  $p$  represents the perpendicular distance of the mass  $dm$  to the axis OL. The graphical representation of the value  $1/\sqrt{I_{OL}}$  for different orientations of the axes OL is an ellipse in 2D and an ellipsoid in 3D according to the associated Equation (Beer et al. 2004; Marghitu and Dupac 2012) as depicted in Figure 2(a). The minor and major axis of the ellipsoid ( $b$  and  $a$ , respectively) define the degree of anisotropy (DA) of the structure following Equation (2), being the two minor axes allowed to differ in length.

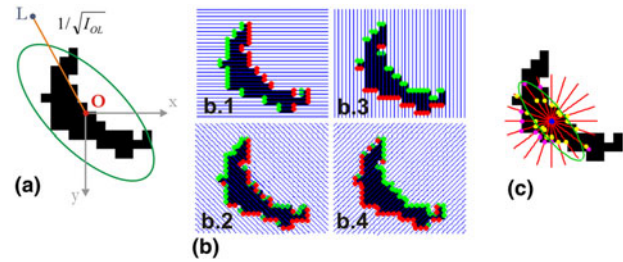


Figure 2. (a) Obtaining of the ellipse of inertia generated on a portion of the CLMA scaffold at the centre of mass O (red point), inverted in colours and zoomed in by a factor of 900 for visual purposes. The graphical representation of the value  $1/\sqrt{I_{OL}}$ , being  $I_{OL}$  the moment of inertia for different orientations of the axis OL, is an ellipse. (b) Illustration of the 2D MIL computed on the same portion of the same scaffold depicted in (a). It is based on the application of straight lines or probes equispaced at different orientation angles. Four orientations are displayed:  $\theta = 0^\circ$  (b.1),  $45^\circ$  (b.2),  $90^\circ$  (b.3) and  $135^\circ$  (b.4) through the binary image. The image is inverted in colours for a better visualisation. Green dots define the white to black transitions and red dots mark the transitions in the opposite order. MIL is calculated by the division between the summation of the length of the blue lines and the number of green dots. (c) Iconography of the 2D t-scale computation at an image point (blue dot) of the same portion of the CLMA scaffold as in (a) and (b). Finally, many radially opposite straight-line segments distributed at uniform angular spacing, called sample lines (red), are traced, and the optimal edge location (magenta dots) is identified on each sample line. Following the axial symmetry of the ellipse, the edge points on every pair of radially outward sample lines are repositioned (yellow dots) by selecting the one closer to the candidate point and then reflecting it onto the opposite sample line. Finally, t-scale is computed by fitting an ellipse (green) to the repositioned edge points. As in (a) and (b), the image is inverted in colours for visual purposes.

$$DA = \frac{a}{b} \quad (2)$$

### Mean intercept length

MIL is a boundary-based method that uses the interface between phases to estimate fabric tensors. With respect to a particular orientation, it is defined as the mean distance between a change from one phase to the other. MIL 2D was based on the application of straight lines or probes equispaced at different orientation angles through a 2D image plane containing binarised objects (Whitehouse 1974). These probes were perpendicular to a main line which rotated at different angles. The probe was rotated while sweeping the binary plane with intermediate angles in order to analyse the line-structure intersections and evaluate the anisotropic orientation patterns. To determine the length of the probes, basic trigonometric relationships were used. The next step was to evaluate the transitions from white to black (binary images) for counting the number of intersections between the probes and the interface between both phases. Finally, the length of the probes was normalised

with respect to the number of transitions from object to background along each of those probes.

After probes rotation, an MIL value was obtained for each angle  $\theta$  defined in the analysis,  $MIL(\theta)$ . The analysis of four orientations to a CLMA scaffold is shown in Figure 2(b). Thus, the results were depicted in polar coordinates ( $MIL(\theta)$ ,  $\theta$ ) and an ellipse was fit to the data using principal component analysis (PCA). This step was accomplished in two substeps: determination of the orientation and computation of the length of the semi-axes. PCA allows to reduce the dimension of a complex problem revealing hidden relationships in data representation. It involves checking if there is any other base that is a linear combination, in which the data are better expressed. To find the optimal base, the original angle must be rotated to maximise the variance and the signal-to-noise ratio. Thus, with PCA, the problem of fitting the data to an ellipsoid turns into how to diagonalise a covariance matrix. The vectors that define the base must be orthonormal, and their directions must match the maximum variation of the acquired data. The DA was obtained following Equation (2) as well.

The extension of the algorithm to its 3D version had certain modifications as it was necessary to obtain a regular distribution of points in the control spherical surface, where the structure under test was enclosed. This consisted in a zonal equal area partitioning (Leopardi 2006), where the area of each region is defined using the Lebesgue measure. In order to obtain a symmetric distribution with respect to the centre of the sphere, the number of points had to be power of two. Then, the central point of each equal area partitioning was joined with the centre of the unit sphere to obtain the direction vector, and extended to the radius of the control sphere to obtain a line. After the structure evaluation, for the adjustment of the edge points to an ellipsoid, an algorithm called minimum volume enclosing ellipsoid (MVEE) was employed (Peng and Freund 2004; Moshtagh 2006). Finally, the value of the minor and major semi-axes allowed calculation of its anisotropy degree. This method is sensitive to outliers; so, an iterative implementation of the Grubbs Test was applied with a significance level of 0.005 for removing outliers (Barnett and Lewis 1994).

The 2D MIL version has three main parameters: the resolution or minimum distance between consecutive points at the same probe, the separation in pixels between consecutive probes and the number of orientations on the plane  $\theta$  that the lines follow. The 3D version has two parameters: the resolution and the number of equal-area regions on the sphere.

#### Tensor scale

The t-scale method, a volume-based method that computes anisotropy from measures taken inside only one phase,

was considered as a new concept of a local morphometric scale using a tensor model (Saha 2003). Conceptually, the t-scale at any image point  $p$  is the parametric representation of the largest ellipse in 2D or ellipsoid in 3D centred at  $p$  that is contained in the same homogeneous region (Saha and Wehrli 2004b).

For a better understanding of the purpose of each step in the detailed description, a schematic illustration of the 2D method is shown in Figure 2(c). Despite illustrating the process using binary images, it is applicable to greyscale images as well (only non-zero pixels are taken into account). As illustrated in the Figure (negative version of the original one for visual purposes), a set of pairs of radially opposite straight-line segments, called sample lines, was superimposed. All of them were uniformly distributed along the angular variable  $\theta$ . Each sample line emanated from the point  $p$ , and the closer edge on each line was detected in order to constitute the local contour of the structure. If none of the evaluated points belonged to the edge, it was set as the last point of the sample line. The distance between  $p$  and a point on the edge was obtained by a parametric integral over the sample line from  $p$  to the first point at which the intensity was equal to 0 (background).

After locating all the edge points, it was necessary to reposition one on each sample line in order to have symmetrical conditions with respect to the central point  $p$  so as to fit the ellipse. Thus, the point closer to  $p$  remained in that position, while the opposite became symmetrical with respect to  $p$ . This can be better understood seeing Figure 2(c). Finally, the t-scale was determined by computing the best-fit ellipse to these repositioned edge points by means of PCA.

Once the t-scale was calculated for each point of the image, parametric maps were built. The colour coding scheme HSV, specifically hue (H), saturation (S) and value (V) of the colour at any pixel  $p$  encodes orientation, anisotropy and thickness, respectively. This model consists of cylindrical-coordinate representations that correspond with a hexagon or cone. According to the coding convention, colours near the centre of the disk represent locally isotropic structures, whereas those near the periphery represent highly anisotropic structures. In order to employ HSV colour space, a slight modification was necessary because with the standard version, an orientation of  $\theta$  will have a different hue than  $\theta + \pi$ . The adopted solution consisted of concentrating all the possible hues between 0 and  $\pi$ , instead of 0 and  $2\pi$  like the standard. For this aim, a condition of symmetry with respect to the revolution axis of the cone was applied as depicted in Figure 3(a). The same portion of the CLMA scaffold studied in Figure 2 is codified in HSV in Figure 3(b). The DA was calculated by means of Equation (2).

The first step for the 3D version, as was the case in the 2D version, was to determine which voxels belonged to the

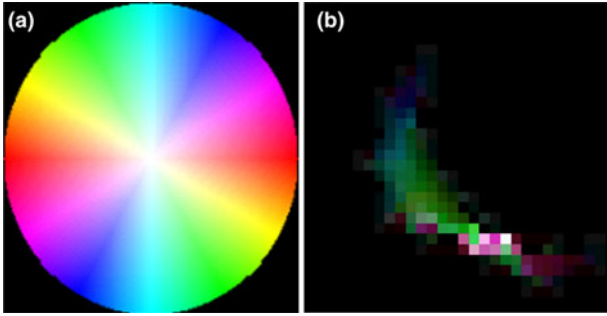


Figure 3. (a) Disk that represents the HSV colours with restriction of symmetry employed in this study, at full intensity. As the hue varies from 0 to 1, the corresponding colours vary from red through yellow, green, cyan, blue, magenta and back to red. Moreover, as saturation varies from 0 to a unit value, the corresponding colours (hues) vary from unsaturated (shades of grey) to fully saturated (no white component). The values equal to 1 correspond with the brighter colours. (b) Parametric representation in colour of the same portion of CLMA scaffold studied in Figure 2, after applying the t-scale method. The colour of each pixel corresponds with the colour whose strip has the same orientation on the HSV disk that the ellipse centred at that pixel.

structure. This required overlaying a set of pairs radially opposite and evenly distributed over the angular variables  $\theta$  (azimuth) and  $\varphi$  (elevation) sample lines. The next step was to determine the coordinates of the points on the local edge of the structure around the point  $p$ , the necessary readjustment and the calculation of the best-fitting ellipsoid by means of least squares. The quantity of structure was calculated by a line integral over the segment defined between the point  $p$  and each point on the edge. The last step of the algorithm was the setting of an ellipsoid to the surface calculated by means of MVEE.

The number of pixels considered on each sample line for the calculation of t-scale determines the degree of locality, which is the maximum distance that is taken into account for calculating the t-scale at  $p$ ,  $p$  being the point for calculating the ellipse. Other important parameters involved in the t-scale method are the resolution or separation between points of the same line and the number of radially opposed sample line pairs on the plane  $\theta$ . For the 3D approach, the same parameters as for the 2D version are maintained, taking into account that now  $p$  is a 3D coordinate, origin of the ellipsoid, and a new parameter appears determining the number of sample line pairs on the angular plane  $\varphi$ .

### Statistical analysis

Statistical analysis was performed for the two groups (CLMA and D scaffolds) after testing normal distribution with the Kolmogorov–Smirnov test using GraphPad Prism (GraphPad Software, Inc., La Jolla, USA). The

student *t*-test was used to compare the two groups with every algorithm (EI, MIL and t-scale). As three comparisons were performed, establishing  $p < (0.05/3) \approx 0.016$  as statistically significant, a Bonferroni adjustment was made. Results are expressed as mean difference and 95% confidence interval (CI) of this difference. Anisotropy data often have skewed distributions; therefore, a result from standard tests based on normality assumptions may not be appropriate for small group comparisons (Henderson 2005) and for this reason, bootstrap method was chosen. The non-parametric bootstrap method is a resampling approach that successively recreates the data sample (repeated samples) by random selection (with replacement) from the original sample, from which values of interest such as average differences are computed (Wood 2004; Mousavi et al. 2011). Bootstrap estimations of differences with the 95% confidence limits were calculated using the 2.5 and 97.5 percentiles of the computed bootstrap average difference in 1000 resamples (Wood 2004).

### Results

A preliminary study has been carried out applying the three described methods to the three well-known simulated 3D patterns: a sphere, an isotropic cube and an anisotropic prism. The dependency of the results obtained by the different methods with the form and the size of the analysed region as well as its own parameters of MIL and t-scale has been studied in depth. The results obtained for each method were compared to the largest possible rectangular ROI and the biggest possible square ROI. The results suggested that the shape of the employed ROI affected the values of the calculated semi-axes, obtaining a higher DA when a square region was used. Thus, in order to use the same amount of information in the three coordinate axes, a square ROI was finally chosen. Concerning the study focused on the size, it consisted of comparing the results obtained with the largest possible square ROI (100%), and three other square regions with sizes 75%, 50% and 25% of the original one (the four regions had the same centre). The size had no influence on the values of the semi-axes of the ellipses and ellipsoids as long as it had enough information of the organisation of the structure. For the scale factors of 100%, 75% and 50%, the values of the semi-axes remained constant, but there was a little change (<6%) for the scale factor of 25% due to the lack of sufficient information to perform the calculations. Taking into account these results, square ROIs of the largest possible size were employed.

For the concrete case of MIL, the separation between lines had no influence on the results as long as a sufficiently dense mesh was provided. However, the resolution affected the values of the semi-axes fundamentally and



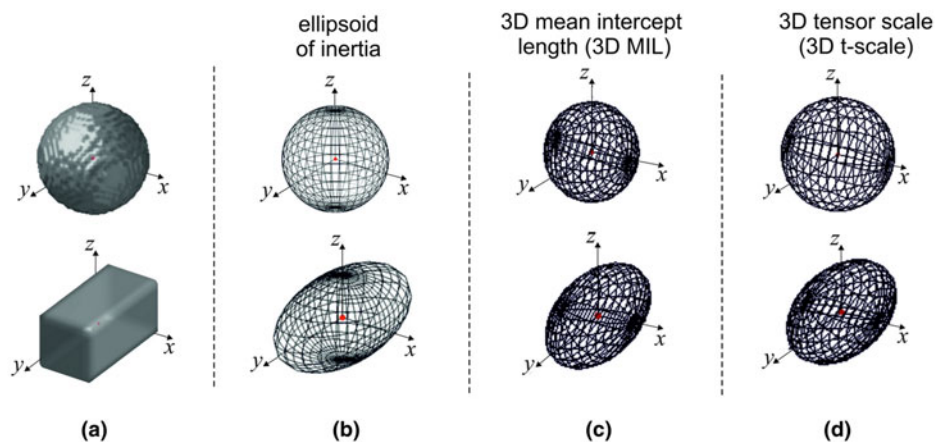


Figure 4. (a) Sphere and prism for the evaluation of the EI and the 3D versions of the MIL and the t-scale methods. (b) Surface generated by the EI method. (c) Ellipsoid generated from the MIL method (from which the DA is calculated). (d) Corresponding ellipsoid of the t-scale method. For all the methods and in the case of the sphere, the resulting surface is almost spherical instead of ellipsoidal, owing to its isotropy. In the case of the prism, as observed visually, the obtained surface is anisotropic.

therefore the obtained DA. There was a tendency to overestimate the distance of the line intercepted by the structure with the deterioration of resolution. On the other hand, the drawback of lines with very close points was the increment of computational time. The resolution was set 0.1, and the control sphere was divided into  $2^{13}$  equal-area regions. The method of the MVEE was applied with a tolerance level of 0.001, and Grubbs Test was established with a significance level of 0.005 for determination of outliers (very few and isolated). For the t-scale method, segments become a collection of points and, therefore, the computational load and the precision of the algorithm depended on the separation between the points over the same line and on the maximum length of such segments. The right choice of the resolution was determined by a trade-off between the computational complexity and the scale of the finest detectable structure. A low resolution was used to obtain enough precision in the calculation of the local contour. So, if a value adequately high for the length was chosen, the obtained results were independent of this variable. If a larger value was used, it increased the computational burden, but the extra information was often not crucial. A resolution of 0.5 pixels was set, as recommended (Xu et al. 2009), 0.5–1 times the smallest dimension of a pixel as well as a length of 10 pixels, fitting into the interval recommended (Saha 2003), i.e. between 8 and 15 pixels. The number of sample line pairs on the angular plane  $\theta$  was 36, and 18 pairs were employed on the angular plane  $\varphi$ .



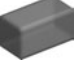
The ellipsoids generated for the three presented methods for the sphere and the prism are depicted in Figure 4. The numerical results concerning DA for the three simulated patterns are listed in Table 1. The obtained results are very similar to the theoretical DA (1 for the isotropic patterns and 2 for the prism 1:1:2) for those simulated structures.

For the case of the scaffolds, every variable was normally distributed, and results are shown in Table 2. EI did not differentiate between the two models, with a difference of means of 0.0158 and 95% CI of  $[-0.5683; 0.6001]$  and a  $p$  value of 0.9435. The MIL method showed no statistically significant differences, between CLMAs and Ds scaffolds: 0.3509  $[0.0656; 0.6362]$ ,  $p = 0.02$ . T-scale depicted high differences between both scaffolds families, 0.3441  $[0.1779; 0.5102]$ ,  $p = 0.004$ .

## Discussion

Regarding the extension of the 2D MIL and t-scale algorithms to a 3D version, several difficulties emerge when considering the spatial domain. It is not correct to generalise MIL from the 2D case as it is necessary to obtain a regular distribution of points on the control spherical surface. The main differences for the implementation of the 3D t-scale version arise from the ellipsoid fitting process and the representation of the results. In the 2D version, the adjustment of the ellipse to the data was calculated using PCA, which was based on a statistical

Table 1. DA obtained by the three methods (EI, MIL and t-scale) applied to three simulated patterns.

			
Theoretical DA	1	1	2
EI	1	1	2.0094
MIL	1.0174	1.0311	1.9647
T-scale	1.0023	1.1093	2.0174

Notes: The first row shows the theoretical anisotropy index for each pattern (taking into account its axis ratio).

Table 2. DA obtained for six scaffolds of two different topologies (four [CLMAx] and two [Dx]) by means of the EI, MIL and t-scale methods.

	CLMA	CLMA70	CLMA50	CLMA30	CLMAx mean [95% CI]	D80	D150	Dx mean [95% CI]
EI	2.6019	2.4932	2.3035	2.7487	2.5368 [2.4890; 2.5822]	2.2653	2.7766	2.5209 [2.2653; 2.7766]
MIL	1.3118	1.6610	1.7043	1.6256	1.5745 [1.5309; 1.6172]	1.2312	1.2183	1.2246 [1.2230; 1.2264]
T-scale	1.4409	1.5008	1.4599	1.4590	1.4649 [1.4588; 1.4704]	1.2137	1.0284	1.1211 [1.0964; 1.1494]

Notes: The difference between the columns containing the means with the CIs for each scaffold topology shows the ability of each method to differentiate them. EI did not differentiate between the two models 0.0158 [−0.5683; 0.6001] (mean and 95% CI),  $p = 0.9435$ . On the other hand, MIL showed no statistically significant differences between CLMAs and Ds scaffolds: 0.3509 [0.0656; 0.6362],  $p = 0.02$ . Significant differences were found with t-scale, 0.3441 [0.1779; 0.5102],  $p = 0.004$ .

analysis of the position of the points to fit in order to estimate the principal direction of the ellipse. From that direction, the ellipse was rotated such that the points could be repositioned to adjust with the canonical formula of a conical section. However, when performing a rotation in 3D, the rotational axis must be specified. Furthermore, this rotation can be decomposed into a series of rotations with respect to the coordinate axes, and although the directions of the principal semi axes of the ellipsoid can be similarly estimated to 2D, the number of rotations required in 3D increases largely. For this reason, a broader adjustment formula was employed based on least squares instead of PCA, which contained implicit definitions of the possible rotations of the ellipsoid with respect to the coordinate axes. For the ellipsoid obtained for each voxel, the least squares method was applied rather than MVEE as it is a faster algorithm. As the MVEE is very sensitive to outliers, an outlier-removal function was applied for the MIL method, and as the t-scale is a more local algorithm, it was necessary to apply this outlier-removal function for this latter case.

As depicted in Figure 4, the sphere generates a geometric figure almost spherical instead of an ellipsoid because of its isotropy, whereas the prism leads to an ellipsoid due to its anisotropy. When meshes that are homogeneous in their mass distribution on macroscopic scales are analysed, it is predictable that this measure will be always one for a sample VOI with an EI–DA of 1.

The DA obtained with all the 3D methods for the cube and sphere is very close to 1 and for the prism is approximately 2 as expected. EI resulted in the fastest method and provided the most accurate results for the patterns.

If the variables are normally distributed, as in this case, the habitual statistic is the mean with a CI of this difference, which by convention is 95% (Wood 2004). Particularly, the major difference in mean DA between the two scaffold topologies is searched. CIs are quoted only for the mean values because 1000 resamples are considered with bootstrap, but not for the rest of values in Table 2 since the measurement is taken only once for each type of scaffold. Bootstrap techniques enable calculation of 95% CIs even with two variables

(Ds scaffolds), which can coincide with maximum and minimum values.

Regarding biopolymer scaffolds, EI was expected to be good due to its accuracy with patterns, but it could not handle complex structures. MIL was much faster than t-scale and the results for patterns were similar, but with the scaffolds, it resulted in no statistical significance. On the other hand, t-scale is a local method and it provided statistically significant differences among the different scaffold structures.

## Conclusions

Three different methods for the analysis of the DA have been compared in three dimensions: the EI, the MIL and the t-scale.

T-scale has provided the best results to differentiate two different scaffold topologies such as cylindrical orthogonal pore mesh and spherical pores, after having proved a high accuracy with simulated 3D patterns.

Although the implemented methods have been applied to scaffold images obtained using a Computed Tomography scanner, they could also have been applied to other types of biomedical images, such as magnetic resonance images, for example.

The design of scaffolds for tissue engineering must follow biomimetic criteria to successfully replace damaged biological structures. This involves a broad range of parameters such as pore size, pore interconnectivity, total porosity, mechanical properties and surface characteristics. A topological parameter that has been long neglected is the anisotropy degree of the designed scaffold, which must be equally considered among design parameters, even more considering that most of tissues are anisotropic in nature (e.g. bone), and synthetic structures should also mimic this property. Scaffold anisotropy represents a critical design feature in the fabrication of musculoskeletal tissues, such as bone, cartilage, muscle, tendons and ligaments, which display a peculiar spatial organisation that results in highly anisotropic mechanical behaviour. This paper has developed a robust methodology to quantify the DA of synthetic scaffolds as a new tool to be used in the design and characterisation of scaffolds.



Because the analysis can be similarly done on the original tissue to be replaced, the methodology allows the engineering of 3D biomimetic scaffolds incorporating advanced properties of the original structure to be replaced, seeking to incorporate the complex natural behaviour into the designed structure.

## Acknowledgements

The support of the Spanish Ministry of Science and Innovation through project TEC2009-14128 is acknowledged.

## References

- Alberich-Bayarri A, Moratal D, Escobar Ivirico JL, Rodríguez Hernández JC, Vallés-Lluch A, Martí-Bonmatí L, Mas Estellés J, Mano JF, Monleón Pradas M, Gómez Ribelles JL, et al., 2009. Microcomputed tomography and microfinite element modeling for evaluating polymer scaffolds architecture and their mechanical properties. *J Biomed Mater Res B Appl Biomater*. 91B(1):191–202.
- Barnett V, Lewis T. 1994. *Outliers in statistical data*. Chichester: John Wiley & Sons.
- Beer FP, Johnston ER, Jr, Eisenberg ER, Clausen WE, Staab GH. 2004. *Vector mechanics for engineers, statics and dynamics*. 7th ed. New York: McGraw Hill. p. 512–544.
- Bokhari M, Carnachan RJ, Przyborski SA, Cameron NR. 2007. Emulsion-templated porous polymers as scaffolds for three dimensional cell culture: effect of synthesis parameters on scaffold formation and homogeneity. *J Mater Chem*. 17 (38):4088–4094.
- Bonani W, Maniglio D, Motta A, Tan W, Migliaresi C. 2011. Biohybrid nanofiber constructs with anisotropic biomechanical properties. *J Biomed Mater Res B Appl Biomater*. 96B (2):276–286.
- Cai X, Chen L, Jiang T, Shen X, Hu J, Tong H. 2011. Facile synthesis of anisotropic porous chitosan/hydroxyapatite scaffolds for bone tissue engineering. *J Mater Chem*. 21 (32):12015–12025.
- Engelmayr GC, Jr, Papworth GD, Watkins SC, Mayer JE, Jr, Sacks MS. 2006. Guidance of engineered tissue collagen orientation by large-scale scaffold microstructures. *J Biomech*. 39(10):1819–1831.
- Escobar Ivirico JL, Costa Martínez E, Salmerón Sánchez M, Muñoz Criado I, Gómez Ribelles JL, Monleón Pradas M. 2007. Structure and properties of methacrylate-endcapped caprolactone networks with modulated water uptake for biomedical applications. *J Biomed Mater Res B Appl Biomater*. 83B(1):266–275.
- Gao CY, Wang DY, Shen JC. 2003. Fabrication of porous collagen/chitosan scaffolds with controlling microstructure for dermal equivalent. *Polym Adv Technol*. 14(6):373–379.
- Garrigues NW, Little D, O'Connor CJ, Guilak F. 2010. Use of an insulating mask for controlling anisotropy in multilayer electrospun scaffolds for tissue engineering. *J Mater Chem*. 20(40):8962–8968.
- Giardino R, Aldini NN, Fini M, Tanzi MC, Fare S, Draghi L, Carpi A, Nicolini A, Giavaresi G. 2006. Bioabsorbable scaffold for *in situ* bone regeneration. *Biomed Pharmacother*. 60(8):386–392.
- Gomberg BR, Saha PK, Wehrli FW. 2003. Topology-based orientation analysis of trabecular bone networks. *Med Phys*. 30(2):158–168.
- Harrigan TP, Mann RW. 1984. Characterization of microstructural anisotropy in orthotropic materials using a second rank tensor. *J Mater Sci*. 19(3):761–767.
- Harris LD, Kim BS, Mooney DJ. 1998. Open pore biodegradable matrices formed with gas foaming. *J Biomed Mater Res*. 42 (3):396–402.
- Henderson AR. 2005. The bootstrap: a technique for data-driven statistics. Using computer-intensive analyses to explore experimental data. *Clin Chim Acta*. 359(1–2):1–26.
- Ho ST, Hutmacher DW. 2006. A comparison of micro CT with other techniques used in the characterization of scaffolds. *Biomaterials*. 27(8):1362–1376.
- Hollister SJ. 2005. Porous scaffold design for tissue engineering. *Nat Mater*. 4(7):518–524.
- Hutmacher DW. 2000. Scaffolds in tissue engineering bone and cartilage. *Biomaterials*. 21(24):2529–2543.
- Inglis D, Pietruszczak S. 2003. Characterization of anisotropy in porous media by means of linear intercept measurements. *Int J Solids Struct*. 40(5):1243–1264.
- Langer R, Vacanti JP. 1993. Tissue engineering. *Science*. 260 (5110):920–926.
- Leopardi P. 2006. A partition of the unit sphere into regions of equal area and small diameter. *Electron Trans Numer Anal*. 25:309–327.
- Li W, Mauck RL, Cooper JA, Yuan X, Tuan RS. 2007. Engineering controllable anisotropy in electrospun biodegradable nanofibrous scaffolds for musculoskeletal tissue engineering. *J Biomech*. 40(8):1686–1693.
- Marghitu DB, Dupac M. 2012. *Advanced dynamics: analytical and numerical calculations with MATLAB*. New York: Springer.
- Mathieu LM, Mueller TL, Bourban PE, Pioletti DP, Müller R, Månson JA. 2006. Architecture and properties of anisotropic polymer composite scaffolds for bone tissue engineering. *Biomaterials*. 27(6):905–916.
- Mikos AG, Sarakinos G, Leite SM, Vacanti JP, Langer R. 1993. Laminated 3-dimensional biodegradable foams for use in tissue engineering. *Biomaterials*. 14(5):323–330.
- Moroni L, de Wijn JR, van Blitterswijk CA. 2006. 3D fiber-deposited scaffolds for tissue engineering: influence of pores geometry and architecture on dynamic mechanical properties. *Biomaterials*. 27(7):974–985.
- Moshtagh N. 2006. Minimum volume enclosing ellipsoids, Technical Report University of Pennsylvania, PA.
- Mousavi SM, Tavakkoli-Moghaddam R, Hashemi H, Mojtahedi SMH. 2011. A novel approach based on non-parametric resampling with interval analysis for large engineering project risks. *Saf Sci*. 49(10):1340–1348.
- Otsu N. 1979. A threshold selection method from gray-level histogram. *IEEE Trans Syst Man Cybern C Appl Rev*. 9 (1):62–66.
- Peng S, Freund RM. 2004. Computation of minimum volume covering ellipsoids. *Oper Res*. 52(5):690–706.
- Rodríguez Hernández JC, Serrano Aroca A, Gómez Ribelles JL, Monleón Pradas M. 2008. Three-dimensional nanocomposite scaffolds with ordered cylindrical orthogonal pores. *J Biomed Mater Res B Appl Biomater*. 84B(2):541–549.
- Saha PK. 2003. Novel theory and methods for tensor scale: a local morphometric parameter. *Med Imaging: Image Processing*. 5032(1–3):743–753.
- Saha PK. 2005. Tensor scale: a local morphometric parameter with applications to computer vision and image processing. *Comput Vis Image Underst*. 99(3):384–413.

- Saha PK, Udupa JK. 2001. Scale-based diffusive image filtering preserving boundary sharpness and fine structures. *IEEE Trans Med Imaging*. 20(11):1140–1155.
- Saha PK, Udupa JK, Odhner D. 2000. Scale-based fuzzy connected image segmentation: theory, algorithms, and validation. *Comput Vis Image Underst*. 77(2):145–174.
- Saha PK, Wehrli FW. 2004a. *In vivo* assessment of trabecular bone architecture via three-dimensional tensor scale. *Med Imaging: Physiol, Func, Struct Med Images*. 5(23):750–760.
- Saha PK, Wehrli FW. 2004b. A robust method for measuring trabecular bone orientation anisotropy at *in vivo* resolution using tensor scale. *Pattern Recognit*. 37(9):1935–1944.
- Salerno A, Iannace S, Netti PA. 2008. Open-pore biodegradable foams prepared via gas foaming and microparticulate templating. *Macromol Biosci*. 8(7):655–664.
- Subramanian A, Krishnan UM, Sethuraman S. 2011. Fabrication of uniaxially aligned 3D electrospun scaffolds for neural regeneration. *Biomed Mater*. 6(2).
- Terrier A, Sedighi-Gilani M, Ghias AR, Aschwanden L, Pioletti DP. 2009. Biomechanical evaluation of porous biodegradable scaffolds for revision knee arthroplasty. *Comput Methods Biomech Biomed Eng*. 12(3):333–339.
- Thomson RC, Wake MC, Yaszemski MJ, Mikos AG. 1995. Biodegradable polymer scaffolds to regenerate organs. *Adv Polym Sci*. 122:245–274.
- Treharne AJ, Grossel MC, Lotery AJ, Thomson HA. 2011. The chemistry of retinal transplantation: the influence of polymer scaffold properties on retinal cell adhesion and control. *Br J Ophthalmol*. 95(6):768–773.
- Wald MJ, Vasilic B, Saha PK, Wehrli FW. 2007. Spatial autocorrelation and mean intercept length analysis of trabecular bone anisotropy applied to *in vivo* magnetic resonance imaging. *Med Phys*. 34(3):1110–1120.
- Wehrli FW. 2007. Structural and functional assessment of trabecular and cortical bone by micro magnetic resonance imaging. *J Magn Resonan Imaging*. 25(2):390–409.
- Whitehouse WJ. 1974. The quantitative morphology of anisotropic trabecular bone. *J Microsc*. 101(2):153–168.
- Wood M. 2004. Statistical inference using bootstrap confidence intervals. *Significance*. 1(4):180–182.
- Xu Z, Sonka M, Saha PK. 2009. Recent improvements in tensor scale computation and its applications to medical imaging. *Med Imaging: Image Process*.
- Xu Z, Sonka M, Saha PK. 2011. Improved tensor scale computation with application to medical image interpolation. *Comput Med Imaging Graph*. 35(1):64–80.
- Yi W, Heo M, Lee S, Choi S, Huh K, Lee S. 2007. Direct measurement of trabecular bone anisotropy using directional fractal dimension and principal axes of inertia. *Oral Surg Oral Med Oral Pathol Oral Radiol Endod*. 104(1):110–116.
- Zhou QL, Gong YH, Gao CY. 2005. Microstructure and mechanical properties of poly(L-lactide) scaffolds fabricated by gelatin particle leaching method. *J Appl Polym Sci*. 98(3):1373–1379.